

Implicit Image-to-Image Schrödinger Bridge for Image Restoration

Yuang Wang^{a,b}, Siyeop Yoon^b, Pengfei Jin^b, Matthew Tivnan^b, Sifan Song^b,
Zhennong Chen^b, Rui Hu^b, Li Zhang^a, Quanzheng Li^b, Zhiqiang Chen^a, Dufan Wu^{b,*}

^a*The Department of Engineering Physics, Tsinghua University, 30 Shuangqing Road, Haidian, Beijing, 100084, China*

^b*Center for Advanced Medical Computing and Analysis, Massachusetts General Hospital and Harvard Medical School, 55 Fruit Street, Boston, MA 02114, Massachusetts, USA*

Abstract

Diffusion-based models are widely recognized for their effectiveness in image restoration tasks; however, their iterative denoising process, which begins from Gaussian noise, often results in slow inference speeds. The Image-to-Image Schrödinger Bridge ($I^2\text{SB}$) presents a promising alternative by starting the generative process from corrupted images and leveraging training techniques from score-based diffusion models. In this paper, we introduce the Implicit Image-to-Image Schrödinger Bridge ($I^3\text{SB}$) to further accelerate the generative process of $I^2\text{SB}$. $I^3\text{SB}$ reconfigures the generative process into a non-Markovian framework by incorporating the initial corrupted image into each step, while ensuring that the marginal distribution aligns with that of $I^2\text{SB}$. This allows for the direct use of the pretrained network from $I^2\text{SB}$. Extensive experiments on natural images, human face images, and medical images validate the acceleration benefits of $I^3\text{SB}$. Compared to $I^2\text{SB}$, $I^3\text{SB}$ achieves the same perceptual quality with fewer generative steps, while maintaining equal or improved fidelity to the ground truth.

Keywords: Image Restoration; Diffusion Model; Schrödinger Bridge

1. Introduction

Restoring high-quality images is a common yet challenging task in both natural and medical imaging. Recently, conditional diffusion models [1, 2, 3] have shown promising performance in addressing this challenge. Rooted in stochastic process theories, diffusion models offer a more stable approach to sampling from complex distributions compared to Generative Adversarial Networks (GANs) [4]. However, the inference speed of diffusion models is often limited by the large number of iterative denoising steps needed to generate clean images starting from pure Gaussian noise.

Instead of starting from Gaussian noise, Schrödinger Bridges establish diffusion bridges [5, 6] between the distributions of clean and corrupted images. By initiating the

*Corresponding author.

Email address: dwu6@mgh.harvard.edu (Dufan Wu)

diffusion process with the corrupted image, which is closer to the clean one than Gaussian noise, Schrödinger Bridges offer a promising approach to generate high-quality conditional samples with fewer diffusion steps. As a special case, the Image-to-Image Schrödinger Bridge (I²SB) [7] models the diffusion path between paired clean and corrupted samples, enabling efficient training by connecting it with score-based diffusion models. The number of neural function evaluations (NFE) in its generative process controls the trade-off between perceptual quality and fidelity to the ground truth [8]. With a small NFE, I²SB tends to produce less distortion but smoother images due to the “regression to the mean effect” [9], whereas with a large NFE, I²SB can generate images with high perceptual quality at the expense of some distortion from the ground truth.

In this work, our aim is to accelerate I²SB to achieve the same perceptual quality and equal or better fidelity to the ground truth with fewer generative steps. Inspired by the success of incorporating non-Markovian processes into the denoising diffusion probabilistic model (DDPM) [10] to create the denoising diffusion implicit model (DDIM) [11], we proposed the Implicit Image-to-Image Schrödinger Bridge (I³SB). Our approach employs a non-Markovian process during inference by incorporating the initial corrupted image into each step alongside the current image and the estimated mean. By constraining the marginal distribution to match that of I²SB, the proposed I³SB shares the same training loss functions with I²SB and can thus reuse pretrained I²SB models. We introduced a single parameter to balance the Markovian and non-Markovian components. Additionally, we established a connection between I³SB and the probability flow ordinary differential equation (PF-ODE) of the Variance Exploded (VE) endpoint-fixed Schrödinger Bridge [12, 13]. I³SB was validated in super-resolution and JPEG restoration tasks using both natural and human face images, as well as in CT sparse view reconstruction, super-resolution, and denoising tasks using medical images.

2. Preliminaries

Notation: Let $X_t \in \mathbb{R}^d$ represent a d -dimensional stochastic process indexed by $t \in [0, 1]$, and N denote the number of generative steps. We denote the discrete generative time steps as $0 = t_0 < \dots < t_n \dots < t_N = 1$, and shorthand $X_n \equiv X_{t_n}$.

2.1. Image-to-Image Schrödinger Bridge

The I²SB [7] establishes direct diffusion bridges between paired clean and corrupted images. With X_0 representing clean images and X_1 representing corresponding corrupted images, X_t is designed to follow the Gaussian distribution $q(X_t|X_0, X_1)$:

$$q(X_t|X_0, X_1) = \mathcal{N}\left(X_t; \frac{\bar{\sigma}_t^2}{\sigma_1^2}X_0 + \frac{\sigma_t^2}{\sigma_1^2}X_1, \frac{\sigma_t^2\bar{\sigma}_t^2}{\sigma_1^2}I\right), \quad (1)$$

where $\sigma_t^2 = \int_0^t \beta_\tau d\tau$ and $\bar{\sigma}_t^2 = \int_t^1 \beta_\tau d\tau$ represent variances accumulated from either side, $\sigma_1^2 = \int_0^1 \beta_\tau d\tau$, and β_τ determines the speed of diffusion. Since X_t can be sampled

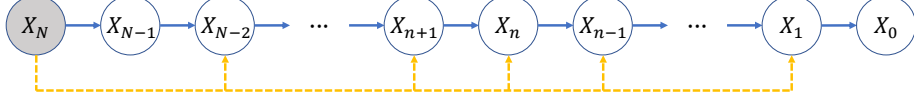


Figure 1: Non-Markovian generative process of I^3SB . Solid arrows denote original dependencies in I^2SB , and dotted arrows signify additional dependencies in I^3SB .

analytically using equation (1), the network ϵ_θ can be efficiently trained to predict the difference between X_t and X_0 by minimizing the loss function:

$$\theta^* = \arg \min_{\theta} \mathbb{E}_{X_0, X_1} \mathbb{E}_{t, X_t} \|\epsilon_\theta(X_t, t) - \frac{X_t - X_0}{\sigma_t}\|, \quad (2)$$

where $t \sim \mathcal{U}[0, 1]$ and $X_t \sim q(X_t | X_0, X_1)$.

In the generative process, I^2SB begins with the corrupted image X_N and iteratively approaches the clean image X_0 . In the step from X_n to X_{n-1} , $\hat{X}_0^{(n)}$, the expected mean of X_0 at time t_n , is first calculated using the trained network ϵ_{θ^*} and X_n :

$$\hat{X}_0^{(n)} = X_n - \sigma_n \epsilon_{\theta^*}(X_n, t_n), \quad (3)$$

where we use $\sigma_n \equiv \sigma_{t_n}$. Subsequently, X_{n-1} is sampled from the DDPM posterior p described by $\hat{X}_0^{(n)}$ and X_n :

$$X_{n-1} \sim p(X_{n-1} | \hat{X}_0^{(n)}, X_n). \quad (4)$$

Here, the DDPM posterior p is expressed as:

$$p(X_{n-1} | \hat{X}_0^{(n)}, X_n) = \mathcal{N}\left(X_{n-1}; \frac{\alpha_{n-1}^2}{\sigma_n^2} \hat{X}_0^{(n)} + \frac{\sigma_{n-1}^2}{\sigma_n^2} X_n, \frac{\sigma_{n-1}^2 \alpha_{n-1}^2}{\sigma_n^2} I\right), \quad (5)$$

where $\alpha_{n-1}^2 = \int_{t_{n-1}}^{t_n} \beta_\tau d\tau$ denotes the accumulated variance between consecutive time steps t_{n-1} and t_n .

3. Method

3.1. Implicit Image-to-Image Schrödinger Bridge

3.1.1. Motivation

We preserve the training process of I^2SB and aim to accelerate its generative process in our proposed I^3SB . The generative process of I^2SB is essentially a Markovian chain, where X_{n-1} depends solely on X_n given the trained network ϵ_{θ^*} (with $\hat{X}_0^{(n)}$ also being a function of X_n). In this setup, the information in X_N is only used in the first step and may be gradually lost through the Markovian chain. I^3SB fully utilizes the information in X_N by incorporating X_N in each generative step, changing the generative process to a non-Markovian chain, as shown in Figure 1.

Algorithm 1 Generative Process of I³SB

Input: $N, \{t_n\}$, corrupted image X_N , trained network ϵ_{θ^*}

```

for  $n = N$  to 1 do
  Predict  $\hat{X}_0^{(n)}$  using  $\epsilon_{\theta^*}(X_n, t_n)$  and  $X_n$ 
  if  $n == N$  then
    Sample  $X_{n-1}$  from  $p(X_{n-1}|\hat{X}_0^{(n)}, X_n)$ 
  else if  $1 < n < N$  then
    Sample  $X_{n-1}$  from  $p_G(X_{n-1}|\hat{X}_0^{(n)}, X_n, X_N)$ 
  else
     $X_0 = \hat{X}_0^{(n)}$ 
  end if
end for
return  $X_0$ 

```

3.1.2. Algorithm

In the generative step from X_n to X_{n-1} , we first compute $\hat{X}_0^{(n)}$ using equation (3) and then sample X_{n-1} from a distribution p_G :

$$X_{n-1} \sim p_G(X_{n-1}|\hat{X}_0^{(n)}, X_n, X_N), \quad (6)$$

where X_N is included. Following DDIM [11], we design $p_G(X_{n-1}|\hat{X}_0^{(n)}, X_n, X_N)$ as a Gaussian distribution with a linear combination of $\hat{X}_0^{(n)}$, X_n and X_N as its mean and $g_n^2 I$ as its covariance matrix :

$$p_G(X_{n-1}|\hat{X}_0^{(n)}, X_n, X_N) = \mathcal{N}(X_{n-1}; A_n \hat{X}_0^{(n)} + B_n X_n + C_n X_N, g_n^2 I), \quad (7)$$

where A_n , B_n and C_n represent the weights of $\hat{X}_0^{(n)}$, X_n and X_N , respectively, and g_n is a hyperparameter to be discussed later. Since the trained network from I²SB is directly used to predict $\hat{X}_0^{(n)}$ in equation (3), the marginal distribution of I³SB should align with that of I²SB. Specifically, if $\hat{X}_0^{(n)}$ equals to X_0 for any n , X_{n-1} sampled from $p_G(X_{n-1}|X_0, X_n, X_N)$ should follow the distribution of $q(X_{n-1}|X_0, X_N)$. Therefore, the distribution p_G must satisfy the following equation:

$$q(X_{n-1}|X_0, X_N) = \int p_G(X_{n-1}|X_0, X_n, X_N) q(X_n|X_0, X_N) dX_n. \quad (8)$$

Substituting equation (7) into equation (8) with $\hat{X}_0^{(n)}$ equal to X_0 , the weights A_n , B_n

and C_n can be analytically expressed in terms of g_n :

$$A_n = \frac{\bar{\sigma}_{n-1}^2}{\sigma_N^2} - \frac{\bar{\sigma}_n^2}{\sigma_N^2} \frac{\sqrt{\sigma_{n-1}^2 \bar{\sigma}_{n-1}^2 - g_n^2 \sigma_N^2}}{\sigma_n \bar{\sigma}_n}, \quad (9a)$$

$$B_n = \frac{\sqrt{\sigma_{n-1}^2 \bar{\sigma}_{n-1}^2 - g_n^2 \sigma_N^2}}{\sigma_n \bar{\sigma}_n}, \quad (9b)$$

$$C_n = \frac{\sigma_{n-1}^2}{\sigma_N^2} - \frac{\sigma_n^2}{\sigma_N^2} \frac{\sqrt{\sigma_{n-1}^2 \bar{\sigma}_{n-1}^2 - g_n^2 \sigma_N^2}}{\sigma_n \bar{\sigma}_n}. \quad (9c)$$

Therefore, X_{n-1} can be efficiently sampled from $p_G(X_{n-1} | \hat{X}_0^{(n)}, X_n, X_N)$ using:

$$X_{n-1} = \left(\frac{\bar{\sigma}_{n-1}^2}{\sigma_N^2} \hat{X}_0^{(n)} + \frac{\sigma_{n-1}^2}{\sigma_N^2} X_N \right) + \sqrt{\frac{\sigma_{n-1}^2 \bar{\sigma}_{n-1}^2}{\sigma_N^2} - g_n^2 \hat{\epsilon}^{(n)} + g_n \epsilon}, \quad (10)$$

where $\epsilon \sim \mathcal{N}(0, I)$ is Gaussian noise, and $\hat{\epsilon}^{(n)}$ is the normalized estimated Gaussian noise from X_n , defined as:

$$\hat{\epsilon}^{(n)} = \frac{\sigma_N}{\sigma_n \bar{\sigma}_n} \left(X_n - \left(\frac{\bar{\sigma}_n^2}{\sigma_N^2} \hat{X}_0^{(n)} + \frac{\sigma_n^2}{\sigma_N^2} X_N \right) \right). \quad (11)$$

The generative process of I³SB is summarized in Algorithm 1.

3.1.3. Hyperparameter

The term g_n can be freely designed as long as it adheres to the constraint:

$$0 \leq g_n \leq \frac{\sigma_{n-1} \bar{\sigma}_{n-1}}{\sigma_N}, \quad (12)$$

to ensure the meaningfulness of taking the square root in equation (10). The functionality of g_n can be interpreted from multiple aspects: it balances between the Markovian and non-Markovian components, controls the stochasticity of the generative process, and determines the degree of dependence on the deterministic estimate of noise component. When g_n equals to $\frac{\sigma_{n-1} \alpha_{n-1}}{\sigma_n}$ for any n , p_G becomes equivalent to the DDPM posterior p , and the generative process of I³SB reverts to that of I²SB. We parameterized g_n as:

$$g_n = \eta \frac{\sigma_{n-1} \alpha_{n-1}}{\sigma_n}, \quad (13)$$

where η is left as a hyperparameter.

3.1.4. Relevance to PF-ODE

When g_n is set to 0, the generative process becomes fully deterministic. We provide the ODE for the deterministic generative process in Lemma 1 and establish its equivalence to the PF-ODE for the VE endpoint-fixed Schrödinger Bridge in Theorem 1. Proofs are provided in the Appendix A.

Lemma 1. *If g_n is set to 0, then equation (10) can be treated as an Euler discretization of the following ODE:*

$$d \frac{X_t}{\sigma_t \bar{\sigma}_t} = \frac{X_1}{\sigma_1^2} d \frac{\sigma_t}{\bar{\sigma}_t} + \frac{\hat{X}_0^{(t)}(X_t)}{\sigma_1^2} d \frac{\bar{\sigma}_t}{\sigma_t}. \quad (14)$$

Theorem 1. *The ODE (14) is equivalent to the PF-ODE for the VE endpoint fixed Schrödinger Bridge.*

3.2. Implementation Details

We validated our proposed method using three groups of experiments: natural image, human face and medical image experiments.

3.2.1. Natural image experiments

For natural image tasks, we used the pretrained model of I^2SB and evaluated our proposed I^3SB with 10,000 images randomly selected from the validation dataset of ImageNet 256×256 [14]. We tested I^3SB on two types of degradations: 4× super-resolution with bicubic interpolation (sr4x-bicubic) and JPEG restoration with a quality factor of 10 (JPEG-10). The hyperparameter η was set to 0.6.

3.2.2. Human face experiments

For the human face experiments, we conducted two groups of tests. In the first group, we used the CelebA-HQ [15] 512×512 dataset, randomly splitting it into 27,000 images for training and 3,000 images for testing. In the second group, following SR3 [3], we trained our model on the FFHQ [16] 512×512 dataset and tested it on the CelebA-HQ 512×512 dataset to assess its robustness to domain differences between the training and testing datasets. The entire FFHQ 512×512 dataset was used for training, and 10,000 images were randomly selected from the CelebA-HQ 512×512 dataset for testing. We evaluated our method on two types of degradations: sr4x-bicubic and JPEG-10. The hyperparameter η was set to 0 in the sr4x-bicubic task in first group, and set to 0.2 in other tasks.

The neural network $\epsilon_\theta(X_n, t_n)$ we trained is a 2D residual U-Net with the same architecture used in DDPM [10]. We concatenated X_N with X_n along the channel dimension to serve as an additional condition for the network. During training, we used 1000 diffusion time steps with quadratic discretization, and adopted a symmetric scheduling of β_t [6, 17]. The model was trained on randomly cropped patches of size 128×128 and tested on the entire 512×512 images. A batch size of 64 was employed during training, using the Adam algorithm with a learning rate of 8×10^{-5} for 200,000 iterations.

3.2.3. Medical image experiments

For the medical image experiments, we evaluated our method on CT sparse view reconstruction, 4× super-resolution (sr4x) and denoising tasks. For CT sparse view reconstruction and sr4x tasks, we used the RPLHR-CT-tiny dataset [18], consisting of anonymized chest CT volumes. The original CT images served as clean images,

Method	Time (s)	PSNR \uparrow	SSIM \uparrow	LPIPS \downarrow	FID \downarrow
ADM [2]	4.91	27.18	0.7767	0.2484	13.906
DDNM [20]	2.77	<u>27.54</u>	<u>0.7826</u>	0.2514	13.997
DDRM [21]	0.56	27.17	0.7740	0.2730	19.700
Π GDM [22]	9.84	25.48	0.7321	0.2130	4.382
DPS [23]	121.65	25.40	0.6940	0.3178	10.251
I^2 SB [7] (NFE=100)	2.79	25.44	0.7009	0.2598	<u>4.128</u>
I^3 SB (NFE=1)	0.03	29.07	0.8240	<u>0.2368</u>	13.299
I^3 SB (NFE=25)	0.70	25.91	0.7150	0.2568	4.115

Table 1: Quantitative results and computation time (per image) of tested methods for the sr4x-bicubic task of natural image experiments. **Bold**: best, under: second best.

Method	Time (s)	PSNR \uparrow	SSIM \uparrow	LPIPS \downarrow	FID \downarrow
DDRM [24]	5.42	<u>28.50</u>	<u>0.8175</u>	0.2955	19.977
Π GDM [22]	11.39	25.82	0.7349	0.2711	6.137
I^2 SB [7] (NFE=100)	3.31	26.62	0.7530	<u>0.2488</u>	<u>3.871</u>
I^3 SB (NFE=1)	0.03	29.39	0.8400	0.2677	16.977
I^3 SB (NFE=25)	0.84	26.86	0.7597	0.2448	3.764

Table 2: Quantitative results and computation time (per image) of tested methods for the JPEG-10 task of natural image experiments. **Bold**: best, under: second best.

and the corresponding corrupted images were generated using the FBP algorithm with projections from 60 distinct views in a fan beam geometry for the CT sparse view reconstruction task, and by downsampling the clean images by a factor of 4 in the projection domain for the CT sr4x task. We used 40 cases (11,090 slices) for training and 5 cases (1,425 slices) for testing. For the CT denoising task, we utilized the Mayo Grand Challenge dataset [19], which includes anonymized abdominal CT scans from 10 patients (5,936 slices) with matched full-dose data and simulated quarter-dose data. We used data from 8 patients for training and 2 patients for testing in our experiment. We trained the neural network $\epsilon_\theta(X_n, t_n)$ using the same architecture and hyperparameters as in the human face experiments, with η set to 0 during inference.

4. Results

4.1. Quantitative Results

In natural image experiments, we compared I^3 SB with I^2 SB [7], the conditional diffusion model ADM [2], and several diffusion-based plug-and-play models, including DNDM [20], DDRM [21, 24], Π GDM [22], and DPS [23]. For quantitative analysis, we calculated Frechet Inception Distance (FID) [25] and learned perceptual image patch similarities (LPIPS) [26] to evaluate perceptual quality and texture restoration ability, and peak signal-to-noise ratio (PSNR) and structural similarity index measure

(SSIM) to assess fidelity to the ground truth, as detailed in Tables 1 and 2. The experiments were run on a single A100 GPU, and the computation time for all tested methods is included in these tables.

In the sr4x-bicubic task (Table 1), I^3 SB achieved the highest PSNR and SSIM with NFE=1 and the best FID with NFE=25. Compared to 100-step I^2 SB, the 25-step I^3 SB outperformed it with a 0.5 improvement in PSNR, a 0.015 increase in SSIM, a 0.003 reduction in LPIPS, and a 0.01 reduction in FID. Noticeably, I^3 SB offered a fourfold acceleration in computation time while achieving slightly better performance. When compared to ADM, DDNM, and DDRM, I^3 SB with a single generative step delivered superior results, with a PSNR increase of 1.5 to 2, a 0.04 to 0.05 increase in SSIM, a 0.01 to 0.04 decrease in LPIPS, and a 0.6 to 6 decrease in FID. Against DPS, 25-step I^3 SB demonstrated better performance, with a 0.5 improvement in PSNR, a 0.02 increase in SSIM, a 20% reduction in LPIPS, and a 60% reduction in FID. Although IIGDM achieved the best LPIPS in this task, it had a worse FID and was 14 times slower than the 25-step I^3 SB.

In the JPEG-10 task (Table 2), I^3 SB achieved the highest PSNR and SSIM with NFE=1 and the best FID and LPIPS with NFE=25. Compared to 100-step I^2 SB, the 25-step I^3 SB outperforms it with a 0.2 improvement in PSNR, a 0.007 increase in SSIM, a 0.004 reduction in LPIPS, and a 0.1 reduction in FID. Similarly with the sr4x experiment, I^3 SB demonstrated 4 \times acceleration while maintaining slightly a better performance. When compared to DDRM, I^3 SB with a single generative step delivered superior results, with a PSNR increase of 0.9, a 0.02 increase in SSIM, a 0.03 decrease in LPIPS, and a 3-point decrease in FID. Against IIGDM, 25-step I^3 SB demonstrated better performance, with a 1-point improvement in PSNR, a 0.025 increase in SSIM, a 10% reduction in LPIPS, and a 40% reduction in FID.

4.2. FID-NFE and FID-SSIM Curves

To further demonstrate the acceleration effect of I^3 SB, we plotted the FID-NFE and FID-SSIM curves for I^2 SB and I^3 SB in all experiments. These curves are presented in Figure 2 for natural image experiments, Figure 3 for human face experiments, and Figure 4 for medical image experiments.

Similar trends were observed in all the tasks for all the experiments. As shown in the FID-NFE curves, both I^2 SB and I^3 SB exhibited decreasing FID as NFE increased, indicating that more generative steps led to improved perceptual quality for both models. Notably, FID decreased faster in I^3 SB as NFE increased, meaning that I^3 SB achieved the same perceptual quality with fewer generative steps.

The FID-SSIM curves highlighted the trade-off between perceptual quality and fidelity to the ground truth. As FID decreased, signaling improved perceptual quality, SSIM often declined, indicating a reduction in fidelity. This trade-off [8] occurred because generating finer details tends to introduce more distortion. Notably, the FID-SSIM curves for I^3 SB either overlapped with or shifted to the lower right of those for I^2 SB, indicating that when both models achieved similar perceptual quality, I^3 SB provided equal or better fidelity. This demonstrated that I^3 SB accelerated the generative process of I^2 SB, achieving the same perceptual quality with fewer generative steps, without introducing additional distortion from the ground truth.

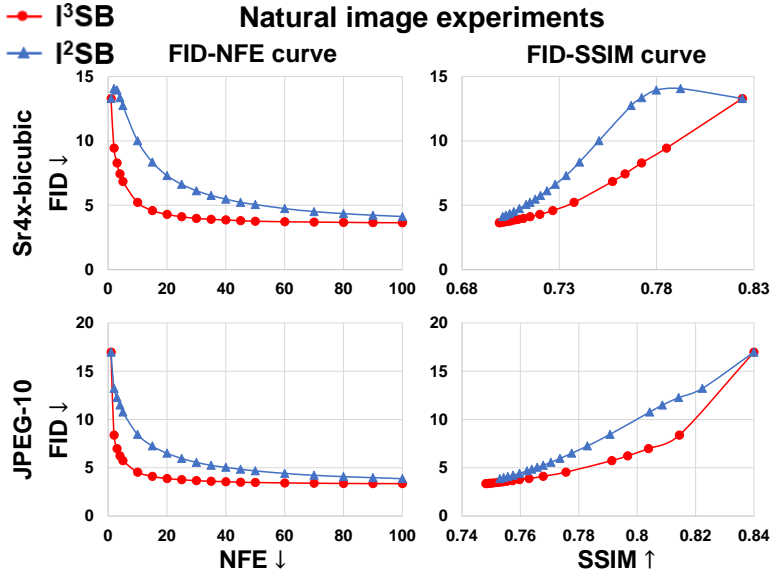


Figure 2: FID-NFE and FID-SSIM curves for sr4x-bicubic and JPEG-10 tasks in natural image experiments. Red denotes the curves of I^3SB , and blue denotes the curves of I^2SB .

Additionally, these trends were consistent when training on the FFHQ dataset and testing on the CelebA-HQ dataset in the human face experiments (Figure 3), indicating that the acceleration impact of I^3SB was robust to domain differences.

In the natural image experiments, I^3SB achieved comparable performance to the 100-step I^2SB using 25 generative steps, resulting in a $4\times$ acceleration. In the human face experiments, I^3SB matched the results of the 100-step I^2SB with 20 to 30 steps, providing a $3\times$ to $5\times$ speedup. For medical image experiments, I^3SB showed a $1.4\times$ to $2\times$ acceleration, achieving similar performance as the 200-step I^2SB with 100 steps in the CT sparse view reconstruction task, and 140 steps in both the CT sr4x and denoising tasks.

4.3. Visualization Results

The superior performance of I^3SB is further demonstrated by the visualization results in Figure 5 and Figure 6 for natural image experiments, Figure 7 for human face experiments, and Figure 8 for medical image experiments. Compared to all comparison methods, I^3SB exhibited enhanced detail restoration across all figures. Specifically, it excelled in restoring finer details, such as text characters, lizard scales, and bird features in Figure 5; the bird's eyes and legs, as well as the dog's nose and tongue in Figure 6, wrinkles, eyelashes, teeth, and nose in Figure 7; and pulmonary veins and mammary glands in Figure 8.

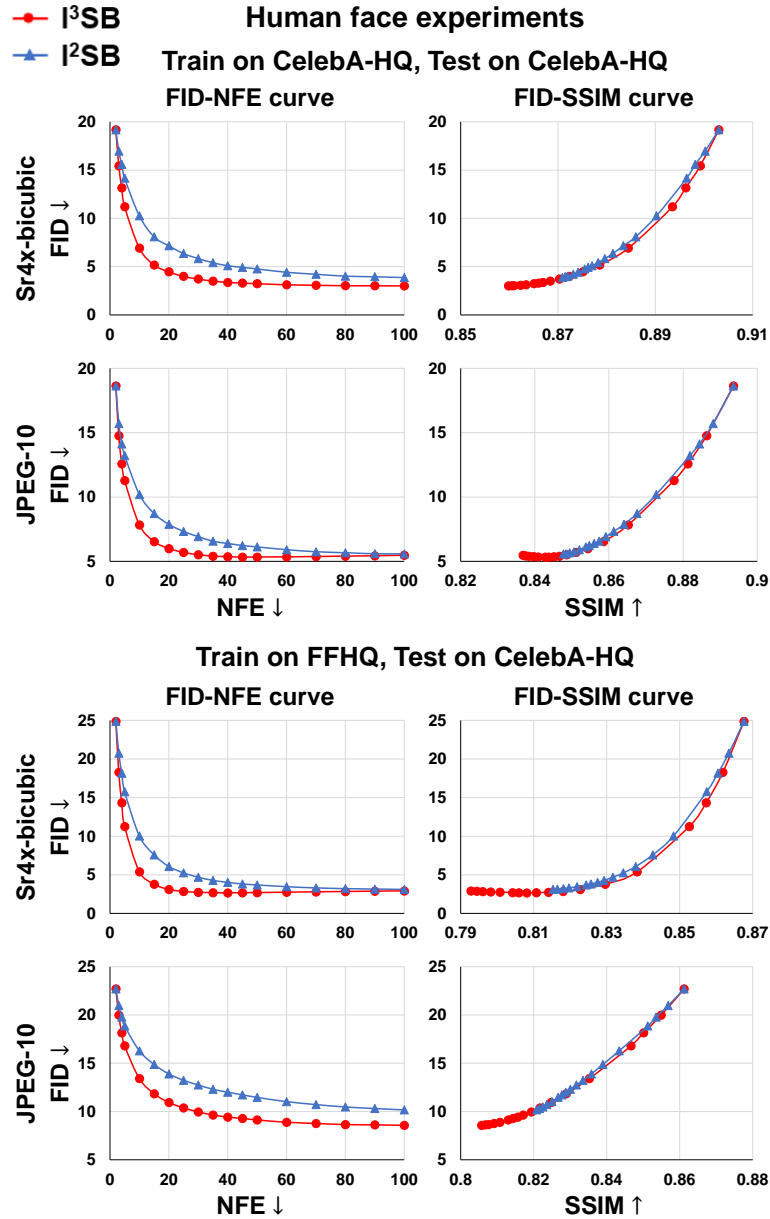


Figure 3: FID-NFE and FID-SSIM curves for sr4x-bicubic and JPEG-10 tasks in human face experiments. Red denotes the curves of I^3SB , and blue denotes the curves of I^2SB .

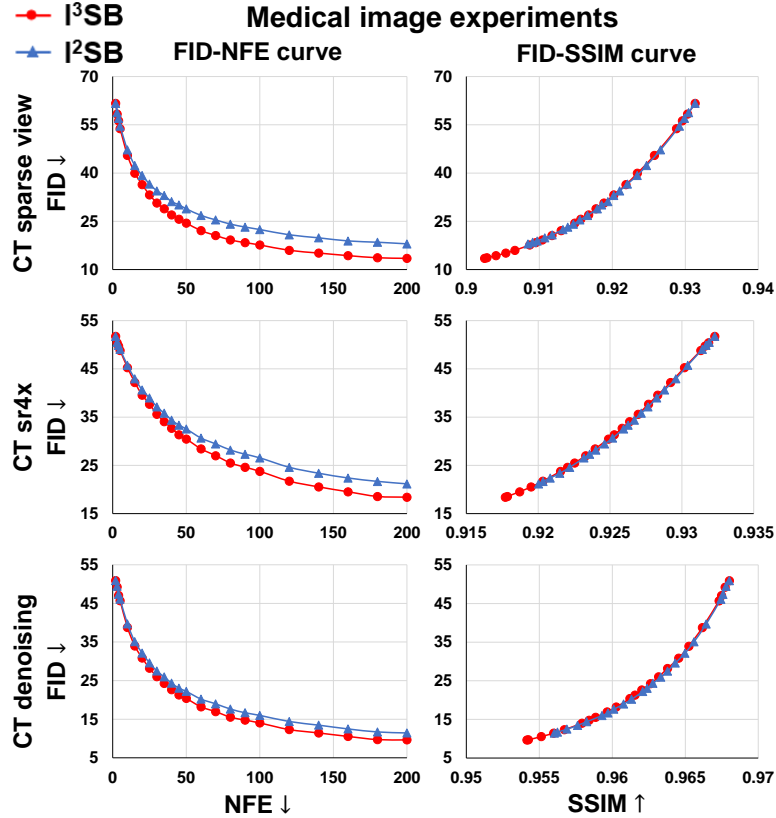


Figure 4: FID-NFE and FID-SSIM curves for CT sparse view reconstruction, sr4x and denoising tasks in medical image experiments. Red denotes the curves of I^3SB , and blue denotes the curves of I^2SB .

5. Related Work

5.1. Diffusion Based Image Restoration Models

Diffusion-based image restoration models can be broadly categorized into task-agnostic and task-specific models. Task-agnostic models train unconditional score functions as priors for the data distribution and incorporate data consistency during inference. These models can be used for various types of corruptions with the same trained network, but they require the specific forward operator corresponding to each corruption during inference. For instance, DDNM [20] and DDRM [21, 24] decompose images into the range and null spaces of the forward operator, applying data consistency to the range space component. MCG [27] employs manifold constraints to determine the gradient tangent to the data distribution manifold, integrating data consistency along this direction. DPS [23] and PIGDM [22] sample from the posterior distribution, using approximations to make the process tractable. Red-Diff [28] formulates image restoration as an optimization problem, incorporating the pretrained score function as a regularization term.

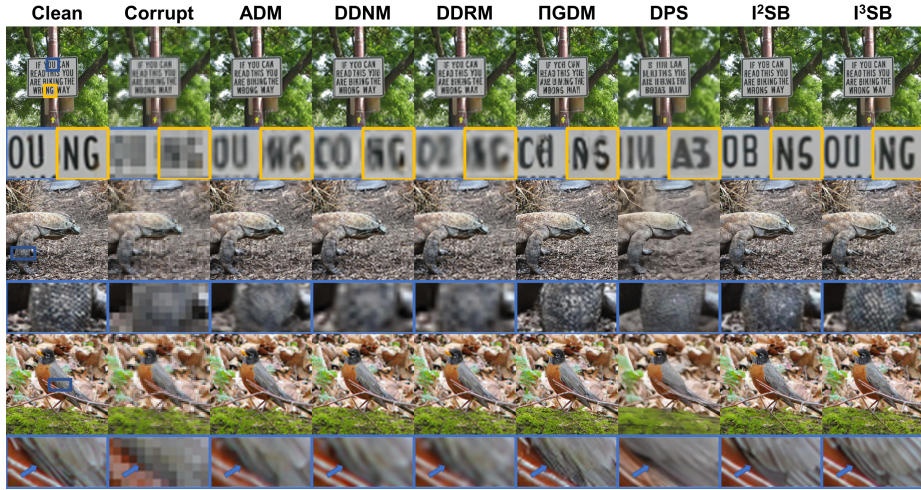


Figure 5: Visualization results of tested methods for the sr4x-bicubic task in the natural image experiments. The details within the blue and yellow boxes are zoomed in for enhanced visual clarity. The NFE for I^2SB is 100, and for I^3SB is 25.

Task-specific models train conditional score functions using the corrupted image as a condition. These models require separate training for each type of corruption, necessitating pairs of clean and corrupted images during training. However, they often outperform task-agnostic models. Moreover, because task-specific models do not need to incorporate additional data consistency during inference, they are capable of handling blind corruption scenarios where the forward operator is unknown. Notable examples of task-specific models include SR3 [3], Palette [1], and ADM [2].

5.2. Acceleration for Diffusion Models

Accelerating the inference process of diffusion models has become a key focus in the field, leading to the development of two main approaches. The first approach involves generating samples by solving the PF-ODE using high-order solvers instead of sampling from stochastic differential equations (SDEs). These methods modify only the inference process without further training the score function. For instance, DDIM [11] accelerates DDPM by transforming the Markovian process into a non-Markovian process and establishes its connection with the PF-ODE. EDM [29] and EDM2 [30] solve the PF-ODE using the Heun’s 2nd order method, achieving state-of-the-art results in image generation. DPM-solver [31] transforms the ODE discretization into a discretization of the exponentially weighted integral of the score function, applying Taylor expansion for approximation. PNDM [32] introduces a manifold-constrained high-order ODE solver, utilizing linear multi-step and Runge-Kutta methods while maintaining intermediate images on the true noisy manifold.

Diffusion distillation is another approach that accelerates the diffusion inference process by leveraging the PF-ODE, which establishes a deterministic mapping between



Figure 6: Visualization results of tested methods for the JPEG-10 task in the natural image experiments. The details within the blue and yellow boxes are zoomed in for enhanced visual clarity. The NFE for I^2SB is 100, and for I^3SB is 25.

Gaussian noise and the final generated images. These methods train student models to distill the multi-step outputs of the original diffusion model into a single step. For example, Progressive Distillation [33] introduces binary time distillation, where the student model is trained to predict the two-step output of the teacher model and then serves as the teacher in the next phase. Consistency Model [34] and TRACT [35] use the student model, equipped with exponentially moving averaged weights, as a self-teacher to incorporate self-consistency into the student model. BOOT [36] eliminates the need for real data during the training of the student model by using the student model’s generated images as inputs for the teacher model.

5.3. Paired Data Schrödinger Bridge

Unlike diffusion models that start from Gaussian noise, Schrödinger Bridges initiate their generative processes from corrupted images, offering a promising alternative for generating high-quality conditional samples with fewer generative steps. Schrödinger Bridges can be broadly categorized into unpaired and paired data Schrödinger Bridges. While unpaired data Schrödinger Bridges [6, 37, 17] often face challenges with inefficient training, paired data Schrödinger Bridges, such as I^2SB [7], InDI [9],

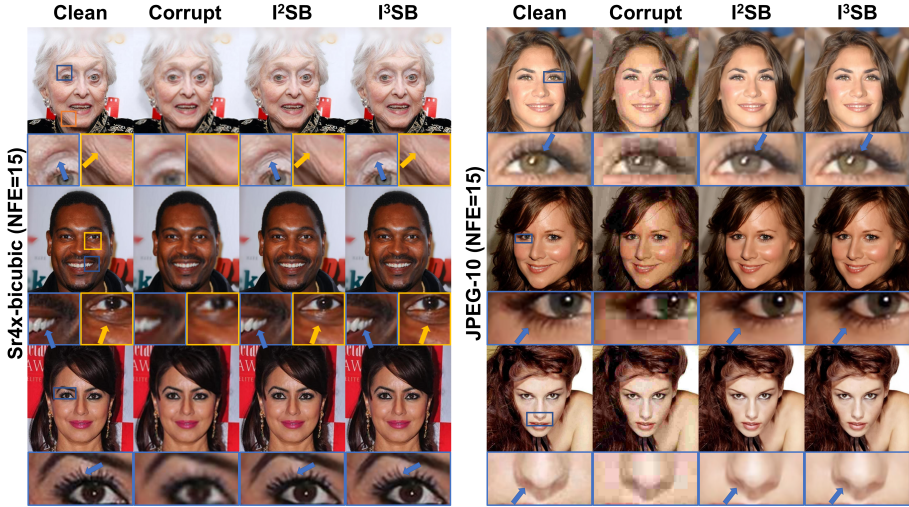


Figure 7: Visualization results for the sr4x-bicubic and JPEG-10 tasks in the first group of human face experiments. The details within the blue and yellow boxes are zoomed in for enhanced visual clarity.

and IR-SDE [38], can be trained as efficiently as score-based diffusion models. Techniques developed for diffusion models have been adapted to paired data Schrödinger Bridges. For instance, DDBM [13] applies Heun’s 2nd-order method to solve the PF-ODE of paired data Schrödinger Bridges and demonstrates good performance in image translation tasks. CDBB [8] enhances I^2SB by incorporating data consistency with techniques from DDS [39] and DPS. Our proposed I^3SB , inspired by DDIM and transforming the generative process from Markovian to non-Markovian, demonstrates acceleration benefits compared to I^2SB .

6. Conclusion and discussion

In conclusion, we introduce I^3SB to accelerate the generative process of I^2SB in image restoration tasks. By incorporating corrupted images into each generative step, I^3SB transitions the generative process into a non-Markovian framework while ensuring that the marginal distribution aligns with that of I^2SB , allowing the use of the same trained network. A single hyperparameter is introduced to balance the Markovian and non-Markovian components. We also establish the equivalence between the deterministic generative process of I^3SB and the PF-ODE for the VE endpoint-fixed Schrödinger Bridge. Our experiments across natural, human face, and medical images demonstrate the significant acceleration benefits of I^3SB . Compared to I^2SB , I^3SB achieves the same perceptual quality with fewer generative steps while maintaining equal or improved fidelity to the ground truth. Furthermore, in natural image experiments, I^3SB surpasses diffusion-based image restoration models, including ADM, DDNM, DDRM, Π GDM, and DPS, in both quantitative metrics and visual quality.

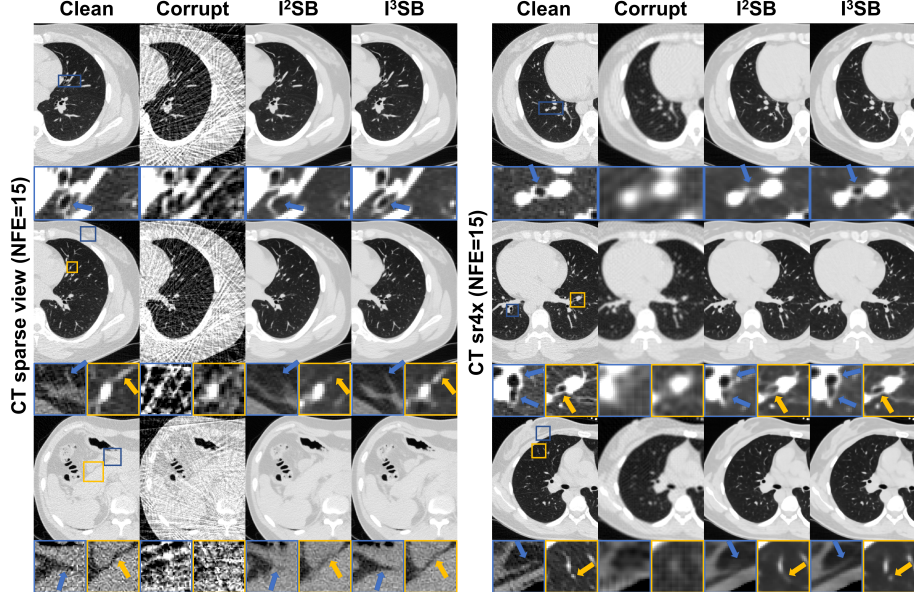


Figure 8: Visualization results for the CT sparse view reconstruction and sr4x tasks in the medical image experiments. The details within the blue and yellow boxes are zoomed in for enhanced visual clarity. The display window for the entire images is set to $[-1000\text{HU}, 200\text{HU}]$, for the zoomed regions outside the lungs is set to $[-160\text{HU}, 200\text{HU}]$, and for the zoomed regions inside the lungs is set to $[-1000\text{HU}, -250\text{HU}]$.

$I^3\text{SB}$ is currently built on the $I^2\text{SB}$ framework, which operates as a VE Schrödinger Bridge. We believe that $I^3\text{SB}$ can be extended to the Variance Preserving (VP) Schrödinger Bridge framework as well. Additionally, since DDIM has been successfully applied in distillation [33] and incorporating data consistency [20, 39, 40], we anticipate that $I^3\text{SB}$ could be similarly adapted for these purposes. These extensions will be explored in our future work.

Appendix A. Proofs

Appendix A.0.1. Proof for equations (9) and (10)

We define $p(X_{n-1}|X_0, X_N)$ as:

$$p(X_{n-1}|X_0, X_N) = \int p_G(X_{n-1}|X_0, X_n, X_N) q(X_n|X_0, X_N) dX_n. \quad (\text{A.1})$$

According to Bishop (2006) [41], $p(X_{n-1}|X_0, X_N)$ is Gaussian, denoted as $\mathcal{N}(X_{n-1}|\mu_{n-1}, \Sigma_{n-1})$ where

$$\mu_{n-1} = A_n X_0 + C_n X_N + B_n \left(\frac{\bar{\sigma}_n^2}{\sigma_N^2} X_0 + \frac{\sigma_n^2}{\sigma_N^2} X_N \right), \quad (\text{A.2a})$$

$$\Sigma_{n-1} = (g_n^2 + B_n^2 \frac{\sigma_n^2 \bar{\sigma}_n^2}{\sigma_N^2}) I. \quad (\text{A.2b})$$

Given equation (8), $p(X_{n-1}|X_0, X_N)$ equals to $q(X_{n-1}|X_0, X_N)$ for any X_{n-1} , X_0 and X_N . Therefore, the weights for X_0 and X_N , as well as the covariance matrix of $p(X_{n-1}|X_0, X_N)$, should match those of $q(X_{n-1}|X_0, X_N)$. This leads to the following equations:

$$\frac{\bar{\sigma}_{n-1}^2}{\sigma_N^2} = A_n + B_n \frac{\bar{\sigma}_n^2}{\sigma_N^2}, \quad (\text{A.3a})$$

$$\frac{\sigma_{n-1}^2}{\sigma_N^2} = C_n + B_n \frac{\sigma_n^2}{\sigma_N^2}, \quad (\text{A.3b})$$

$$\frac{\bar{\sigma}_{n-1}^2 \sigma_{n-1}^2}{\sigma_N^2} = g_n^2 + B_n^2 \frac{\sigma_n^2 \bar{\sigma}_n^2}{\sigma_N^2}. \quad (\text{A.3c})$$

By solving the system of equations in (A.3), we obtain the expressions for A_n , B_n and C_n as given in equation (9).

The sample X_{n-1} is drawn from $p_G(X_{n-1}|\hat{X}_0^{(n)}, X_n, X_N)$ as in equation (6), which gives us:

$$X_{n-1} = A_n \hat{X}_0^{(n)} + B_n X_n + C_n X_N + g_n \epsilon, \quad (\text{A.4})$$

where $\epsilon \sim \mathcal{N}(0, I)$ represents Gaussian noise. By substituting the expressions for A_n , B_n and C_n into equation (A.4), we derive the expression for X_n as shown in equation (10).

Appendix A.0.2. Proof for Lemma 1

When g_n is set to 0, equation (10) simplifies to:

$$X_{n-1} = \left(\frac{\bar{\sigma}_{n-1}^2}{\sigma_N^2} \hat{X}_0^{(n)} + \frac{\sigma_{n-1}^2}{\sigma_N^2} X_N \right) + \frac{\sigma_{n-1} \bar{\sigma}_{n-1}}{\sigma_n \bar{\sigma}_n} \left(X_n - \left(\frac{\bar{\sigma}_n^2}{\sigma_N^2} \hat{X}_0^{(n)} + \frac{\sigma_n^2}{\sigma_N^2} X_N \right) \right). \quad (\text{A.5})$$

This can be rearranged as:

$$\frac{X_{n-1}}{\sigma_{n-1} \bar{\sigma}_{n-1}} - \frac{X_n}{\sigma_n \bar{\sigma}_n} = \left(\frac{\sigma_{n-1}}{\bar{\sigma}_{n-1}} - \frac{\sigma_n}{\bar{\sigma}_n} \right) \frac{X_N}{\sigma_N^2} + \left(\frac{\bar{\sigma}_{n-1}}{\sigma_{n-1}} - \frac{\bar{\sigma}_n}{\sigma_n} \right) \frac{\hat{X}_0^{(n)}}{\sigma_N^2}, \quad (\text{A.6})$$

which can be seen as an Euler discretization of the ODE in equation (14).

Appendix A.0.3. Proof for Theorem 1

To prove Theorem 1, we begin by deriving the PF-ODE for the VE endpoint-fixed Schrödinger Bridge. Following this, we establish its equivalence with the ODE given in equation (14).

The Schrödinger Bridge is an entropy-regularized optimal transport method [42] that constructs diffusion bridges between two arbitrary distributions, p_A and p_B . It is characterized by the following forward and backward SDEs:

$$dX_t = [f_t + \beta_t \nabla_{X_t} \log \Psi(X_t, t)] dt + \sqrt{\beta_t} dw_t, \quad (\text{A.7a})$$

$$dX_t = [f_t - \beta_t \nabla_{X_t} \log \hat{\Psi}(X_t, t)] dt + \sqrt{\beta_t} d\bar{w}_t. \quad (\text{A.7b})$$

Here, X_0 is sampled from p_A , X_1 is sampled from p_B , and w_t and \bar{w}_t denote the Wiener process and its time-reversed counterpart. To ensure that the path measure induced by the forward SDE (A.7a) is almost surely equal to the one induced by the reverse SDE (A.7b), the time-varying energy potentials Ψ and $\hat{\Psi}$ should satisfy the following coupled partial differential equations (PDEs):

$$\frac{\partial \Psi}{\partial t} = -\nabla \Psi^\top f - \frac{1}{2} \beta \Delta \Psi, \quad (\text{A.8a})$$

$$\frac{\partial \hat{\Psi}}{\partial t} = -\nabla \cdot (\hat{\Psi} f) + \frac{1}{2} \beta \Delta \hat{\Psi}, \quad (\text{A.8b})$$

with the marginal conditions:

$$\Psi(X_0, 0) \hat{\Psi}(X_0, 0) = p_A(X_0), \quad (\text{A.9a})$$

$$\Psi(X_1, 1) \hat{\Psi}(X_1, 1) = p_B(X_1). \quad (\text{A.9b})$$

As noted by Chen 2021 [6], the ODE

$$dX_t = \left(f_t + \frac{1}{2} \beta_t \nabla_{X_t} \log \frac{\Psi(X_t, t)}{\hat{\Psi}(X_t, t)} \right) dt \quad (\text{A.10})$$

characterizes the probability flow of the forward and reverse processes of the Schrödinger Bridge defined in equation (A.7).

VE endpoint-fixed Schrödinger Bridge defines f_t , p_A and p_B as follows:

$$f_t = 0, \quad (\text{A.11a})$$

$$p_A(X_0) = q_{\text{clean}}(X_0 | X_{\text{corrupt}}), \quad (\text{A.11b})$$

$$p_B(X_1) = \delta(X_1 - X_{\text{corrupt}}), \quad (\text{A.11c})$$

where X_{corrupt} represents a given corrupted image, and $q_{\text{clean}}(\cdot | X_{\text{corrupt}})$ represents the clean image distribution conditioned on X_{corrupt} . The Dirac function δ indicates that the endpoint fixed Schrödinger Bridge is constructed for each specific corrupted image, rather than for the entire corrupted image distribution.

Lemma 2. *If p_A , p_B and f_t are defined as in equations (A.11), then the PDEs (A.8) with the marginal conditions (A.9) admit the following analytical solutions:*

$$\Psi(X_t, t) = \mathcal{N}(X_t | X_{\text{corrupt}}, \bar{\sigma}_t^2 I), \quad (\text{A.12})$$

$$\hat{\Psi}(X_t, t) = \int \hat{\Psi}_{X_0}(X_t, t) q_{\text{clean}}(X_0 | X_{\text{corrupt}}) dX_0, \quad (\text{A.13})$$

where

$$\hat{\Psi}_{X_0}(X_t, t) = C_{X_0} \mathcal{N}(X_t | X_0, \sigma_t^2 I), \quad (\text{A.14})$$

and

$$C_{X_0} = \left(\sqrt{2\pi} \sigma_1 \right)^d \exp \left(\frac{(X_0 - X_{\text{corrupt}})^T (X_0 - X_{\text{corrupt}})}{2\sigma_1^2} \right). \quad (\text{A.15})$$

Furthermore,

$$\nabla_{X_t} \log \Psi = -\frac{1}{\bar{\sigma}_t^2} (X_t - X_{\text{corrupt}}), \quad (\text{A.16})$$

and

$$\nabla_{X_t} \log \hat{\Psi} = -\frac{1}{\sigma_t^2} (X_t - \hat{X}_0^{(t)}), \quad (\text{A.17})$$

where the expected mean $\hat{X}_0^{(t)}$ is defined as:

$$\hat{X}_0^{(t)} = \int X_0 q_{\text{clean}}(X_0 | X_t, X_{\text{corrupt}}) dX_0. \quad (\text{A.18})$$

Lemma 2 establishes the relationships between $\nabla \log \Psi$, $\nabla \log \hat{\Psi}$, $\hat{X}_0^{(t)}$, X_t and X_{corrupt} . Leveraging these relationships, we prove the equivalence between the ODEs (14) and (A.10). Applying the chain rule, we obtain:

$$d\frac{\sigma_t}{\bar{\sigma}_t} = \frac{\sigma_1^2}{2\sigma_t \bar{\sigma}_t^3} \beta_t dt, \quad (\text{A.19a})$$

$$d\frac{\bar{\sigma}_t}{\sigma_t} = -\frac{\sigma_1^2}{2\sigma_t^3 \bar{\sigma}_t} \beta_t dt, \quad (\text{A.19b})$$

and

$$\begin{aligned} d\frac{X_t}{\sigma_t \bar{\sigma}_t} &= \frac{1}{\sigma_t \bar{\sigma}_t} dX_t + X_t d\frac{1}{\sigma_t \bar{\sigma}_t}, \\ &= \frac{1}{\sigma_t \bar{\sigma}_t} dX_t + X_t \frac{\sigma_t^2 - \bar{\sigma}_t^2}{2\sigma_t^3 \bar{\sigma}_t^3} \beta_t dt. \end{aligned} \quad (\text{A.20})$$

Substituting equations (A.19) and (A.20) into equation (14), we find that the ODE (14) is equivalent to:

$$dX_t = \frac{1}{2} \beta_t \left(\frac{1}{\bar{\sigma}_t^2} (X_1 - X_t) + \frac{1}{\sigma_t^2} (X_t - \hat{X}_0^{(t)}) \right) dt. \quad (\text{A.21})$$

Using $X_1 = X_{\text{corrupt}}$ along with equations (A.11a), (A.16) and (A.17), we conclude that the ODE (14) is equivalent to ODE (A.10), which is the PF- ODE for the VE endpoint fixed Schrödinger Bridge.

Appendix A.0.4. Proof for Lemma 2

To prove Lemma 2, we first demonstrate that Ψ , as defined in equation (A.12), satisfies the PDE (A.8a). This holds because:

$$\begin{aligned}\frac{\partial \Psi}{\partial t} &= \frac{\partial \Psi}{\partial \bar{\sigma}_t^2} \frac{\partial \bar{\sigma}_t^2}{\partial t}, \\ &= -\frac{1}{2} \beta \Psi \left(\frac{(X_t - X_{\text{corrupt}})^T (X_t - X_{\text{corrupt}})}{\bar{\sigma}_t^4} - \frac{d}{\sigma_t^2} \right), \\ &= -\frac{1}{2} \beta \Delta \Psi.\end{aligned}\quad (\text{A.22})$$

Similarly, $\hat{\Psi}_{X_0}(X_t, t)$ satisfies: $\frac{\partial \hat{\Psi}_{X_0}}{\partial t} = \frac{1}{2} \beta \Delta \hat{\Psi}_{X_0}$. Consequently, $\hat{\Psi}$ expressed in equation (A.13) satisfies:

$$\begin{aligned}\frac{\partial \hat{\Psi}}{\partial t} &= \int \frac{\partial \hat{\Psi}_{X_0}}{\partial t} q_{\text{clean}}(X_0 | X_{\text{corrupt}}, y) dX_0, \\ &= \frac{1}{2} \beta \int \Delta \hat{\Psi}_{X_0} q_{\text{clean}}(X_0 | X_{\text{corrupt}}, y) dX_0, \\ &= \frac{1}{2} \beta \Delta \hat{\Psi}.\end{aligned}\quad (\text{A.23})$$

Therefore, Ψ and $\hat{\Psi}$ satisfy the PDEs (A.8).

Next, we proof that Ψ and $\hat{\Psi}$ satisfy the marginal conditions (A.9). At $t = 0$, we have

$$\Psi(X_0, 0) = 1/C_{X_0}, \quad (\text{A.24})$$

where C_{X_0} is defined in equation (A.15). Additionally,

$$\begin{aligned}\hat{\Psi}(X_0, 0) &= \int C_X \delta(X_0 - X) q_{\text{clean}}(X | X_{\text{corrupt}}) dX, \\ &= C_{X_0} q_{\text{clean}}(X_0 | X_{\text{corrupt}}).\end{aligned}\quad (\text{A.25})$$

Therefore, the marginal condition (A.9a) holds. At $t = 1$, we have

$$\Psi(X_1, 1) = \delta(X_1 - X_{\text{corrupt}}), \quad (\text{A.26})$$

and since $\hat{\Psi}_{X_0}(X_1 = X_{\text{corrupt}}, 1)$ equals 1, we have:

$$\begin{aligned}\Psi(X_1, 1) \hat{\Psi}(X_1, 1) &= \delta(X_1 - X_{\text{corrupt}}) \int \hat{\Psi}_{X_0}(X_1, 1) q_{\text{clean}}(X_0 | X_{\text{corrupt}}) dX_0, \\ &= \delta(X_1 - X_{\text{corrupt}}) \int q_{\text{clean}}(X_0 | X_{\text{corrupt}}) dX_0, \\ &= \delta(X_1 - X_{\text{corrupt}}), \\ &= p_B(X_1).\end{aligned}\quad (\text{A.27})$$

Thus, Ψ and $\hat{\Psi}$ expressed in equations (A.12) and (A.13) satisfy the marginal conditions (A.9).

Finally, we provide proofs for equations (A.16) and (A.17). For equation (A.16), $\nabla_{X_t} \log \Psi$ can be straightforwardly obtained by direct computation. For equation (A.17), we proceed as follows:

$$\begin{aligned}
\nabla \log \hat{\Psi} &= \frac{\nabla \hat{\Psi}}{\hat{\Psi}} \\
&= \frac{1}{\hat{\Psi}} \int \nabla \hat{\Psi}_{X_0}(X_t, t) q_{\text{clean}}(X_0|X_{\text{corrupt}}) dX_0 \\
&= \frac{1}{\hat{\Psi}} \int \left(\frac{X_0 - X_t}{\sigma_t^2} \right) \hat{\Psi}_{X_0} q_{\text{clean}}(X_0|X_{\text{corrupt}}) dX_0 \\
&= -\frac{1}{\sigma_t^2} \left(X_t - \frac{1}{\hat{\Psi}} \int X_0 \hat{\Psi}_{X_0} q_{\text{clean}}(X_0|X_{\text{corrupt}}) dX_0 \right)
\end{aligned} \tag{A.28}$$

Using the definition of $\hat{\Psi}_{X_0}$ in equation (A.14), we have:

$$\hat{\Psi}_{X_0}(X_t, t) = k_{X_t} q(X_t|X_0, X_1 = X_{\text{corrupt}}), \tag{A.29}$$

where $q(X_t|X_0, X_1)$ is defined in equation (1), and k_{X_t} is independent of X_0 . Since X_1 is sampled from a Dirac distribution centered at X_{corrupt} , we obtain:

$$q(X_t|X_0, X_1 = X_{\text{corrupt}}) = q(X_t|X_0, X_{\text{corrupt}}). \tag{A.30}$$

Therefore:

$$\nabla \log \hat{\Psi} = -\frac{1}{\sigma_t^2} \left(X_t - \frac{\int X_0 q(X_t|X_0, X_{\text{corrupt}}) q_{\text{clean}}(X_0|X_{\text{corrupt}}) dX_0}{\int q(X_t|X_0, X_{\text{corrupt}}) q_{\text{clean}}(X_0|X_{\text{corrupt}}) dX_0} \right) \tag{A.31}$$

Using Bayes' theorem, we know that:

$$q(X_t|X_0, X_{\text{corrupt}}) = \frac{q_{\text{clean}}(X_0|X_t, X_{\text{corrupt}}) q(X_t|X_{\text{corrupt}})}{q_{\text{clean}}(X_0|X_{\text{corrupt}})}. \tag{A.32}$$

Thus, we have

$$\begin{aligned}
\nabla \log \hat{\Psi} &= -\frac{1}{\sigma_t^2} \left(X_t - \frac{\int X_0 q_{\text{clean}}(X_0|X_t, X_{\text{corrupt}}) dX_0}{\int q_{\text{clean}}(X_0|X_t, X_{\text{corrupt}}) dX_0} \right) \\
&= -\frac{1}{\sigma_t^2} (X_t - \hat{X}_0^{(t)}).
\end{aligned} \tag{A.33}$$

That completes the proof.

Declaration of generative AI and AI-assisted technologies in the writing process

During the preparation of this work the authors used ChatGPT in order to improve language and readability. After using this tool, the authors reviewed and edited the content as needed and take full responsibility for the content of the publication.

Acknowledgements

The authors acknowledge financial support provided by National Institute of Biomedical Imaging and Bioengineering and Samsung Electronics Co., Ltd.

References

- [1] C. Saharia, W. Chan, H. Chang, C. Lee, J. Ho, T. Salimans, D. Fleet, M. Norouzi, Palette: Image-to-image diffusion models, in: ACM SIGGRAPH 2022 conference proceedings, 2022, pp. 1–10.
- [2] P. Dhariwal, A. Nichol, Diffusion models beat gans on image synthesis, *Advances in neural information processing systems* 34 (2021) 8780–8794.
- [3] C. Saharia, J. Ho, W. Chan, T. Salimans, D. J. Fleet, M. Norouzi, Image super-resolution via iterative refinement, *IEEE Transactions on Pattern Analysis and Machine Intelligence* 45 (2022) 4713–4726.
- [4] X. Wang, L. Xie, C. Dong, Y. Shan, Real-esrgan: Training real-world blind super-resolution with pure synthetic data, in: Proceedings of the IEEE/CVF international conference on computer vision, 2021, pp. 1905–1914.
- [5] B. Kim, G. Kwon, K. Kim, J. C. Ye, Unpaired image-to-image translation via neural schrödinger bridge, *arXiv preprint arXiv:2305.15086* (2023).
- [6] T. Chen, G.-H. Liu, E. A. Theodorou, Likelihood training of schrödinger bridge using forward-backward sdes theory, *arXiv preprint arXiv:2110.11291* (2021).
- [7] G.-H. Liu, A. Vahdat, D.-A. Huang, E. A. Theodorou, W. Nie, A. Anandkumar, I^2 sb: Image-to-image schrödinger bridge, *arXiv preprint arXiv:2302.05872* (2023).
- [8] H. Chung, J. Kim, J. C. Ye, Direct diffusion bridge using data consistency for inverse problems, *Advances in Neural Information Processing Systems* 36 (2024).
- [9] M. Delbracio, P. Milanfar, Inversion by direct iteration: An alternative to denoising diffusion for image restoration, *arXiv preprint arXiv:2303.11435* (2023).
- [10] J. Ho, A. Jain, P. Abbeel, Denoising diffusion probabilistic models, *Advances in neural information processing systems* 33 (2020) 6840–6851.
- [11] J. Song, C. Meng, S. Ermon, Denoising diffusion implicit models, *arXiv preprint arXiv:2010.02502* (2020).
- [12] Y. Song, J. Sohl-Dickstein, D. P. Kingma, A. Kumar, S. Ermon, B. Poole, Score-based generative modeling through stochastic differential equations, *arXiv preprint arXiv:2011.13456* (2020).
- [13] L. Zhou, A. Lou, S. Khanna, S. Ermon, Denoising diffusion bridge models, *arXiv preprint arXiv:2309.16948* (2023).

- [14] J. Deng, W. Dong, R. Socher, L.-J. Li, K. Li, L. Fei-Fei, Imagenet: A large-scale hierarchical image database, in: 2009 IEEE conference on computer vision and pattern recognition, Ieee, 2009, pp. 248–255.
- [15] T. Karras, Progressive growing of gans for improved quality, stability, and variation, arXiv preprint arXiv:1710.10196 (2017).
- [16] T. Karras, S. Laine, T. Aila, A style-based generator architecture for generative adversarial networks, in: Proceedings of the IEEE/CVF conference on computer vision and pattern recognition, 2019, pp. 4401–4410.
- [17] V. De Bortoli, J. Thornton, J. Heng, A. Doucet, Diffusion schrödinger bridge with applications to score-based generative modeling, *Advances in Neural Information Processing Systems* 34 (2021) 17695–17709.
- [18] P. Yu, H. Zhang, H. Kang, W. Tang, C. W. Arnold, R. Zhang, Rplhr-ct dataset and transformer baseline for volumetric super-resolution from ct scans, in: International Conference on Medical Image Computing and Computer-Assisted Intervention, Springer, 2022, pp. 344–353.
- [19] AAPM, Low dose ct grand challenge, [Online], 2017. Available: <http://www.aapm.org/GrandChallenge/LowDoseCT/>.
- [20] Y. Wang, J. Yu, J. Zhang, Zero-shot image restoration using denoising diffusion null-space model, arXiv preprint arXiv:2212.00490 (2022).
- [21] B. Kawar, M. Elad, S. Ermon, J. Song, Denoising diffusion restoration models, *Advances in Neural Information Processing Systems* 35 (2022) 23593–23606.
- [22] J. Song, A. Vahdat, M. Mardani, J. Kautz, Pseudoinverse-guided diffusion models for inverse problems, in: International Conference on Learning Representations, 2023.
- [23] H. Chung, J. Kim, M. T. Mccann, M. L. Klasky, J. C. Ye, Diffusion posterior sampling for general noisy inverse problems, arXiv preprint arXiv:2209.14687 (2022).
- [24] B. Kawar, J. Song, S. Ermon, M. Elad, Jpeg artifact correction using denoising diffusion restoration models, arXiv preprint arXiv:2209.11888 (2022).
- [25] M. Heusel, H. Ramsauer, T. Unterthiner, B. Nessler, S. Hochreiter, Gans trained by a two time-scale update rule converge to a local nash equilibrium, *Advances in neural information processing systems* 30 (2017).
- [26] R. Zhang, P. Isola, A. A. Efros, E. Shechtman, O. Wang, The unreasonable effectiveness of deep features as a perceptual metric, in: Proceedings of the IEEE conference on computer vision and pattern recognition, 2018, pp. 586–595.
- [27] H. Chung, B. Sim, D. Ryu, J. C. Ye, Improving diffusion models for inverse problems using manifold constraints, *Advances in Neural Information Processing Systems* 35 (2022) 25683–25696.

- [28] M. Mardani, J. Song, J. Kautz, A. Vahdat, A variational perspective on solving inverse problems with diffusion models, arXiv preprint arXiv:2305.04391 (2023).
- [29] T. Karras, M. Aittala, T. Aila, S. Laine, Elucidating the design space of diffusion-based generative models, Advances in neural information processing systems 35 (2022) 26565–26577.
- [30] T. Karras, M. Aittala, J. Lehtinen, J. Hellsten, T. Aila, S. Laine, Analyzing and improving the training dynamics of diffusion models, in: Proceedings of the IEEE/CVF Conference on Computer Vision and Pattern Recognition, 2024, pp. 24174–24184.
- [31] C. Lu, Y. Zhou, F. Bao, J. Chen, C. Li, J. Zhu, Dpm-solver: A fast ode solver for diffusion probabilistic model sampling in around 10 steps, Advances in Neural Information Processing Systems 35 (2022) 5775–5787.
- [32] L. Liu, Y. Ren, Z. Lin, Z. Zhao, Pseudo numerical methods for diffusion models on manifolds, arXiv preprint arXiv:2202.09778 (2022).
- [33] T. Salimans, J. Ho, Progressive distillation for fast sampling of diffusion models, arXiv preprint arXiv:2202.00512 (2022).
- [34] Y. Song, P. Dhariwal, M. Chen, I. Sutskever, Consistency models, 2023. URL: <https://arxiv.org/abs/2303.01469>. arXiv:2303.01469.
- [35] D. Berthelot, A. Autef, J. Lin, D. A. Yap, S. Zhai, S. Hu, D. Zheng, W. Talbott, E. Gu, Tract: Denoising diffusion models with transitive closure time-distillation, arXiv preprint arXiv:2303.04248 (2023).
- [36] J. Gu, S. Zhai, Y. Zhang, L. Liu, J. M. Susskind, Boot: Data-free distillation of denoising diffusion models with bootstrapping, in: ICML 2023 Workshop on Structured Probabilistic Inference & Generative Modeling, 2023.
- [37] Y. Chen, T. T. Georgiou, M. Pavon, Stochastic control liaisons: Richard sinkhorn meets gaspard monge on a schrödinger bridge, Siam Review 63 (2021) 249–313.
- [38] Z. Luo, F. K. Gustafsson, Z. Zhao, J. Sjölund, T. B. Schön, Image restoration with mean-reverting stochastic differential equations, arXiv preprint arXiv:2301.11699 (2023).
- [39] H. Chung, S. Lee, J. C. Ye, Decomposed diffusion sampler for accelerating large-scale inverse problems, arXiv preprint arXiv:2303.05754 (2023).
- [40] B. Song, S. M. Kwon, Z. Zhang, X. Hu, Q. Qu, L. Shen, Solving inverse problems with latent diffusion models via hard data consistency, arXiv preprint arXiv:2307.08123 (2023).
- [41] C. M. Bishop, Pattern recognition and machine learning, Springer google schola 2 (2006) 1122–1128.
- [42] C. Léonard, A survey of the schrödinger problem and some of its connections with optimal transport, arXiv preprint arXiv:1308.0215 (2013).